

Plasmon-induced near-infrared fluorescence enhancement of single-walled carbon nanotubes



Amirmostafa Amirjani ^{a, b}, Ted V. Tsoulos ^c, Sayyed Hashem Sajjadi ^b,
Alessandra Antonucci ^b, Shang-Jung Wu ^b, Giulia Tagliabue ^{c, **, *},
Davoud Fatmehsari Haghshenas ^{d, ***, *}, Ardemis A. Boghossian ^{b, *}

^a Department of Materials Science and Engineering, Sharif University of Technology, Tehran, Iran

^b Ecole Polytechnique Fédérale de Lausanne (EPFL), Institute of Chemical Sciences and Engineering, CH-1015 Lausanne, Switzerland

^c Laboratory of Nanoscience for Energy Technologies (LNET), École Polytechnique Fédérale de Lausanne (EPFL), Lausanne, CH-1015, Switzerland

^d Department of Materials and Metallurgical Engineering, Amirkabir University of Technology, Tehran, Iran

ARTICLE INFO

Article history:

Received 8 February 2022

Accepted 15 March 2022

Keywords:

Single-walled carbon nanotubes (SWCNTs)

Nanospheres

Nanotriangles

Nanorods

Plasmonic hot spots

Silver

ABSTRACT

Single-walled carbon nanotubes (SWCNTs) emit near-infrared (NIR) fluorescence that is ideal for optical sensing. However, the low quantum yields diminish the sensor's signal-to-noise ratio and limits the penetration depths for *in vivo* measurements. In this study, we perform a systematic investigation of the plasmonic effects of Ag and Au nanoparticles of various geometries to tune and even enhance the fluorescence intensity of single-stranded DNA-wrapped SWCNTs (ssDNA-SWCNTs). We observe a chirality-dependent NIR fluorescence enhancement that varies with both nanoparticle shape and material, with Au nanorods increasing (7, 5) and (7, 6) chirality emissions by 80% and 60% and Ag nanotriangles increasing (7, 5) and (6, 5) emissions by 200% and 240%, respectively. The chirality-dependent enhancement was modeled using finite element modeling (FEM), which confirms contributions not only from a plasmon-induced localized increase in electron density but also from the radiative recombination of dark exciton states from the resulting electromagnetic field. Finally, we demonstrate the application of these nanoparticles in enhancing the single-molecule fluorescence of individual SWCNTs imaged in a custom-built confocal setup. The plasmonically coupled sensors show four orders of magnitude greater sensitivity towards ferricyanide, a model analyte, compared to the non-coupled sensors. Plasmonic nanoparticles thus provide a tunable means of modulating SWCNT fluorescence to study fundamental transitions of otherwise forbidden states and to improve the optical sensing performance.

© 2022 The Authors. Published by Elsevier Ltd. This is an open access article under the CC BY-NC-ND license (<http://creativecommons.org/licenses/by-nc-nd/4.0/>).

1. Introduction

Plasmonic nanoparticles are metallic nanostructures with dimensions below the wavelength of the incident light. At the resonant frequency, these nanostructures can show extraordinary optical properties, such as tunable and enhanced light absorption and scattering. These optical properties can be altered with particle size, shape, and chemical composition [1–4] across wavelengths that span from the ultraviolet–visible (UV) to the near-infrared II

(NIR-II) region [5,6]. The optical tunability of plasmonic nanoparticles has enabled applications based on phenomena such as Fano resonance, near-field coupling and far-field dipole-dipole interactions, surface-enhanced infrared absorption, as well as surface-enhanced Raman scattering (SERS) and energy harvesting [7–9].

Among these applications, plasmonic nanoparticles have also been used to enhance the fluorescence properties of optically coupled fluorophores [10,11]. The fluorescence enhancement is achieved by matching the resonant wavelength of the plasmonic nanostructure with the optical properties of the fluorescent dyes. Though several studies have shown enhancement for a variety of fluorophores [12–14], the majority of demonstrations have been confined to the visible range of the optical spectrum. The tunability of these nanoparticles for fluorescence enhancement beyond the

* Corresponding author.

** Corresponding author.

*** Corresponding author.

E-mail addresses: giulia.tagliabue@epfl.ch (G. Tagliabue), dahafa@aut.ac.ir (D.F. Haghshenas), ardemis.boghossian@epfl.ch (A.A. Boghossian).

visible range has remained largely overlooked, particularly in the NIR-II range used for *in vivo* optical imaging [15].

Single-walled carbon nanotubes (SWCNTs) show distinct NIR-II fluorescence that has been demonstrated for *in vivo* imaging and sensing applications [15–18]. The absorption and emission peaks vary with the nanotube diameter in accordance with the specific (n,m) indices corresponding to the nanotube chirality [19,20]. The NIR-II emissions of SWCNTs lie within the optical transparency window of biological materials, where the absorption of bio-fluids and tissues are minimal. Combined with the deep penetration depths at longer wavelengths and indefinite photostability, these emissions show exceptional advantages for continuous, deep-tissue imaging in biological samples [21,22].

One limiting characteristic of SWCNTs is the low fluorescence quantum yields (QYs), which have been reported to lie in the range of 0.1–1.5% in aqueous media [20]. Increased QYs would contribute to deeper imaging penetration depths [23] as well as a possible increase in the sensitivity of optical nanotube sensors, for which brighter nanotubes have shown greater sensitivity [24]. While long, defect-free SWCNTs show the greatest intrinsic QYs, the lack of scalable, reproducible, and accessible SWCNT synthesis procedures have limited their availability. Previous approaches for increasing the QY include metal-enhanced fluorescence [15,25] of SWCNTs that are immobilized on substrate surfaces. Though these studies report over a 10-fold increase in fluorescence, the surface immobilization of the SWCNTs limits their use for solution-phase imaging. The addition of reductive brightening agents, such as Trolox, can also enhance the QY [26], though often at the expense of increased cytotoxicity and reduced sensor sensitivity [27]. Most recent endeavors have focused on defect engineering or doping sites on SWCNTs, which have shown a 20–30% enhancement in fluorescence [28,29].

An alternative approach for enhancing SWCNT optical properties is through plasmonic coupling with metal nanoparticles [30–35]. Plasmonic nanoparticles have been shown to enhance SWCNT Raman scattering [36–38], and this enhancement has been demonstrated in SERS imaging and photothermal therapy applications [37]. Plasmonic Raman enhancements have also been achieved using DNA instead of metal nanoparticles [39]. Although several studies have used plasmonic nanoparticles to enhance the near-infrared fluorescence of various fluorophores [40,41], only a few studies have reported plasmonic enhancement of NIR-II SWCNT fluorescence [42–44]. For example, Glaeske et al. [42,45] examined the effects Au nanorods, reporting up to a 20-fold enhancement [42]. Despite the impressive enhancements, these observations were limited to surfactant-suspended SWCNTs that show limited applications for optical sensing. In addition, Yang et al. [43] have reported a maximum 10-fold enhancement, in this case for ssDNA-SWCNTs in the presence of Au nanospheres through near-field coupling effects. However, the effects of alternative nanoparticle geometries, particularly those with enhanced localized fields, were not explored. The current literature further lacks a systematic study that implements a methodical approach to examining the effect of geometry, composition, and other factors that are crucial for tuning the plasmonic effects. In particular, the effects of triangular Ag nanoparticles, which have shown superior plasmonic properties [46,47], have yet to be reported using SWCNTs. Such a comparative study is crucial for understanding and ultimately modeling and predicting the plasmonic effects on SWCNTs. In addition, and importantly, the application of these plasmonically enhanced SWCNTs for optical sensing has yet to be reported.

In this study, we explore the plasmonic enhancement of NIR-II fluorescence from single-stranded DNA-wrapped SWCNTs (ssDNA-SWCNTs) (Fig. 1) and apply these coupled conjugates for

single-molecule sensing. The ssDNA-SWCNTs represent a rapidly advancing area of research for optical biosensing [48,49] and chirality separation [50]. We herein study the effects of Ag and Au plasmonic nanostructures with the spherical, rod, and triangular morphologies. We further explore the underlying mechanism of plasmon-enhanced fluorescence using finite element modeling (FEM) to simulate the effects of nanoparticle geometry and material, including near-field effects that have been confirmed in previous studies [43].

2. Materials and methods

2.1. Chemicals and nanoparticle synthesis

CoMoCAT SWCNTs were purchased from Chasem, and all ssDNA sequences used in this study were purchased from Microsynth. Sodium iodide (NaI), sodium chloride (NaCl), ascorbic acid (AA), polyvinylpyrrolidone (PVP-K30), sodium borohydride (NaBH_4), chloroauric acid (HAuCl_4), trisodium citrate (TSC), silver nitrate (AgNO_3), and sodium hydroxide (NaOH) were purchased from Sigma-Aldrich. Cetyltrimethylammonium chloride (CTAC) and cetyltrimethylammonium bromide (CTAB) were purchased from Acros, and hydrogen peroxide (H_2O_2) was purchased from Reac-tolab. All measurements were done in analytical triplicate.

2.2. Preparation of ssDNA-SWCNT solution

The ssDNA-SWCNT solutions were prepared using 0.5–1.0 mg/mL CoMoCAT nanotubes with a 2:1 ssDNA:SWCNT ratio in the presence of 0.1 M NaCl. The as-prepared solution was sonicated for 90 min at 1 W followed by centrifugation at 16000 rcf for 4 h to remove the nanotube bundles. The resulting supernatant was extracted for further experiments.

2.3. Preparation of nanoparticles

Au nanospheres were prepared by heating 100 mL of HAuCl_4 (2.5×10^{-4} M) for 10 min. After boiling, 3 mL of freshly-prepared TSC (1% in DI water) was added. The solution continued boiling for 30 min, developing a deep wine red color indicative of nanoparticle formation.

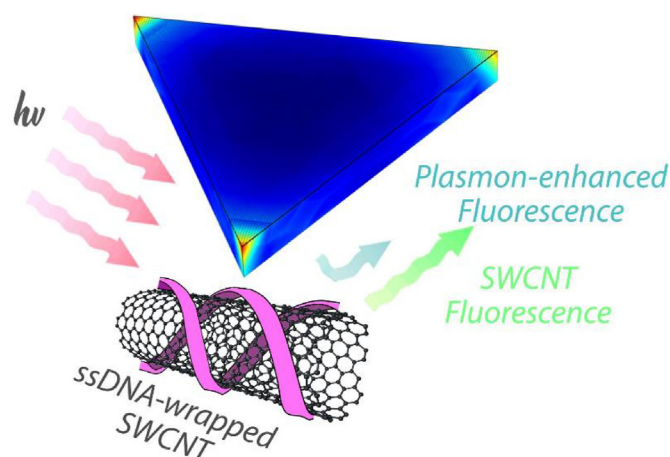


Fig. 1. Schematic of ssDNA-wrapped SWCNT in the vicinity of metallic nanostructures that contribute to plasmon-enhanced fluorescence. Upon illumination at resonant wavelengths (red), the metallic nanoparticles show shape, size, and composition-specific plasmonic effects (blue) for enhancing NIR-II SWCNT fluorescence (green). (A colour version of this figure can be viewed online.)

Ag nanospheres were prepared by adding 50 μL of AgNO_3 (0.1 M) and 50 μL of trisodium citrate (0.1 M) while stirring at 500 rpm to enough DI water to yield a total volume of 20 mL. After 30 min, ice-cooled NaBH_4 (1.2 mL, 25 mM) was added to the above solution. The solution became yellow following NaBH_4 addition, indicative of nanoparticle formation. The solution was stirred at 500 rpm for 30 min.

Ag nanorods were prepared by mixing 2 mL of 2.5 mM AgNO_3 and 2 mL of TSC (2.5 mM). After thorough mixing, 600 μL of NaOH (10 mM) was added, followed by the addition of 20 mL of DI water. 600 μL of NaBH_4 (10 mM) was then added to the solution while stirring. After 2 h, 1 mL of this seed solution was added to a mixture containing 0.25 mL AgNO_3 (10 mM), 0.5 mL ascorbic acid (AA) (100 mM), and 10 mL cetrimonium bromide (CTAB) (50 mM), followed by NaOH (0.1 mL, 1 M) addition. The resulting red color of the solution was indicative of nanoparticle formation.

Au nanorods were prepared by stirring HAuCl_4 (25 μL , 50 mM) and CTAB (4.7 mL, 0.1 M) thoroughly until the solution was no longer turbid. Then, 300 μL of an ice-cold NaBH_4 (10 mM) was rapidly injected under vigorous stirring, and this seed solution was kept at 30 $^\circ\text{C}$. A growth solution was prepared by mixing CTAB (10 mL, 0.1 M), HCl (190 μL , 1 M), HAuCl_4 (100 μL , 50 mM), AgNO_3 (120 μL , 10 mM) and AA (100 μL , 100 mM). 24 μL of the seed solution was added to the growth solution and stirred for 10 min. The resulting mixture was kept at 30 $^\circ\text{C}$ to prevent CTAB crystallization.

Au nanotriangles were prepared using a seed solution, an intermediate solution, and a growth solution. For the seed solution, 25 μL of 0.05 M HAuCl_4 was added to 4.7 mL of 0.1 M CTAC followed by the addition of 300 μL of ice-cooled 0.01 M NaBH_4 . For the intermediate solution, 1.6 mL of 0.1 M CTAC was added to 8 mL of DI water followed by NaBH_4 (40 μL , 0.05 M) and NaI (15 μL , 0.01 M) addition. Finally, for the growth solution, 500 μL of 0.05 M HAuCl_4 was added to 40 mL of 0.05 M CTAC followed by the addition of 300 μL of 0.01 M NaI . The nanoparticles were synthesized by adding 100 μL of the seed solution to 900 μL of CTAC (0.1 M). 40 and 400 μL of AA (0.1 M) were added to the intermediate and growth solutions, respectively, resulting in the transparency of both solutions. 100 μL of diluted seed solution was added to the intermediate solution, and 3.2 mL of this resulting mixture was quickly added to the growth solution. This mixture was incubated at room temperature for 1 h. The resulting blue color of the solution was indicative of nanoparticle formation.

Ag nanotriangles were prepared by rigorously stirring mixtures of AgNO_3 (50 mL, 0.1 mM) and TSC (3 mL, 30 mM) in a 100-mL Erlenmeyer flask. Then, polyvinylpyrrolidone (PVP) (3 mL, 0.7 mM) and H_2O_2 (120 μL , 30% in DI water) were added at room temperature. After 15 min, ice-cooled NaBH_4 (300 μL , 100 mM) was injected into the solution while stirring at 600 rpm. After the addition of NaBH_4 , the color of the solution changed from colorless, to pale yellow, to orange, to red, to indigo, and finally, to blue.

In order to remove the byproducts or unreacted species from the solutions, all of the nanoparticles were washed three times with acetone and one time with DI water. The particles were then centrifuged at 16000 rpm for 1 h. The upper 95% of the supernatant was discarded, and the concentrated particles were extracted and stored at 4 $^\circ\text{C}$ (except for the Au nanorods, which were stored at 30 $^\circ\text{C}$ to prevent crystallization of CTAB).

Since the extinction coefficients of the nanoparticles vary with size and shape, we applied a previously reported technique based on coupled plasma atomic emission spectroscopy (ICP-OES 5110, Agilent) to account for variability in nanoparticle concentration in comparing their plasmonic effects [1,4]. Washed nanoparticle solutions were diluted to have the maximum absorbance of 1 at their maximum surface plasmon resonance wavelength. 1 μL of each sample was digested in HNO_3 (10%). According to the inductively

coupled plasma atomic emission spectroscopy results, the concentration of nanoparticles in all cases was between 0.2 and 0.3 mg/L.

2.4. Preparation of nanoparticle-conjugated ssDNA-SWCNTs

Nanoparticle-conjugated ssDNA-SWCNTs were prepared by mixing 40 μL of a 40-fold dilution of the stock ssDNA-SWCNT solution with 1 μL of nanoparticle solution. Enough DI water was added to yield a total volume of 60 μL (for a final SWCNT:nanoparticle volume ratio of 40:1). The final concentration of SWCNTs in the resulting mixture was 20 mg/L, as estimated from the absorption spectrum ($\epsilon_{780\text{nm}} = 24 \text{ mL mg}^{-1}\text{cm}^{-1}$ [3]). Based on the nanoparticle concentration analysis described above, the amount of nanoparticles in the 60 μL solution following ssDNA-SWCNT conjugation was in the range of 12–18 ng.

2.5. NIR fluorescence spectroscopy

The NIR-II fluorescence spectroscopy and confocal measurements were performed using custom-built setups described in previous work [51]. The setup consists of a super continuum laser source and a tunable band-pass filter unit (SuperK Extreme EXR-15 and SuperK Varia, NKT Photonics) that operates between 400 and 830 nm at a pulse frequency of 80 MHz. A short-pass filter (890 nm blocking edge BrightLine, Semrock) was used to remove NIR reflections. The excitation light was directed into a 20 \times objective (M Plan Apo NIR, NA 0.4 air, Mitutoyo Corporation) using silver-coated mirrors and a dichroic reflector (LP 830 nm, Semrock), resulting in an illumination spot of 350 \times 350 μm . Light emitted from the sample was collected in the epi-direction and focused onto the entrance slit of an IsoPlane SCT-320 spectrometer (Princeton Instruments). A 70 lines mm^{-1} grating was used to disperse the light, which was redirected into an InGaAs NIR camera (NIRvana 640 ST, Princeton Instruments). Measurements were recorded with Light-Field (Princeton Instruments) and custom-built LabView (National Instruments) software. The optical system was calibrated with a NIR calibration source (HL-3plus-CAL-EXT, Omicron Optics) prior to measurement, and wavelength calibration was performed using characteristic lines of a mercury lamp (IntelliCal, Princeton Instruments). The photoluminescence excitation-emission plots were collected using laser excitation at 500–800 nm with 5 nm steps with an exposure time of 5 s per step.

2.6. Absorbance, light scattering and TEM characterizations

Absorbance spectra were acquired with a Shimadzu UV/VIS/NIR scanning spectrometer (3600 Plus) using 50 μL quartz cuvettes. Light scattering measurements were performed using a Nano Zetasizer (Malvern). The samples for the TEM images of the nanoparticles were prepared by dropping 50 μL of each as-prepared nanoparticle solution on copper grids. The samples were imaged at 200 KV (OSIRIS).

2.7. Finite element modeling (FEM)

We modeled the optical properties of the Ag nanotriangles by numerically solving a frequency domain wave equation (Eq. (1)) in the RF (radio frequency) module of COMSOL Multiphysics according to our previously established method [52,53] for linearly polarized illumination (Eq. (2)). The resulting three-dimensional solution for the electric field was integrated over the nanotriangle volume to determine the rate of energy absorption, W_{abs} (Eq. (3)). This rate was divided by the incident irradiance, P_{inc} (Eq. (4)) to obtain the absorption cross section, σ_{abs} (Eq. (5)). The frequency-

dependent relative permittivity ϵ_r was determined based on the work of Johnson and Christy [54]. The relative permeability, μ_r , was set to 1, since the magnetic properties of Ag are negligible in the current system, and Z_0 is the impedance of free space. We account for the frequency-dependent dielectric properties of water as the surrounding medium [55].

$$\nabla \times \frac{1}{\mu_r} (\nabla \times \vec{E}) - k_0^2 \left(\epsilon_r - \frac{j\sigma}{\omega\epsilon_0} \right) \vec{E} = \vec{0} \quad (\text{Eq. 1})$$

$$\vec{E} = e^{-j\vec{k}_0 \cdot \vec{z}} \hat{x} \quad (\text{Eq. 2})$$

$$W_{abs} = \frac{1}{2} \iiint_{xyz} \left[\text{Re} \left[(\sigma \vec{E} + j\omega \vec{D}) \cdot \vec{E}^* \right] + j\omega \vec{B} \cdot \vec{E}^* \right] dx dy dz (W) \quad (\text{Eq. 3})$$

$$P_{inc} = \frac{1}{2Z_0} |\vec{E}_0|^2 (W / m^2) \quad (\text{Eq. 4})$$

$$\sigma_{abs} = \frac{W_{abs}}{P_{inc}} (m^2) \quad (\text{Eq. 5})$$

The tridimensional numerical simulation is based on a concentric spherical domain model, where a single nanoparticle is placed in the center, surrounded by a spherical water domain and enclosed in an ideally absorbing domain with a non-scattering boundary at the outermost limit. A detailed schematic representation is given in Fig. S1 in the SI.

Special considerations were taken to apply a classical electromagnetic approach for atom-thick systems, like graphene [56,57] and carbon nanotubes, which can exhibit singularities. We assumed that the conjugation of SWCNTs in the proximity of the nanoparticles creates an environment with a higher carrier density: while the nm-scale size of the carbon nanotubes has a negligible effect on the plasmonic nanoparticle size, their high electrical conductivity must still be considered. We thus modified the frequency-dependent dielectric function of the Ag nanotriangles (ϵ_{Ag}) using a published analytical model [58]. We observed that a 20% increase of the Ag carrier density alters the plasma frequency in a manner consistent with the experimental results. We thus utilized this modified dielectric function for Ag to model the system in the presence of SWCNTs.

Since the absorption spectrum of the nanotriangle solution varies with nanoparticle thickness, we modeled the distribution of Ag nanotriangle thicknesses by fitting the weighted average sum of the predicted absorption spectra of the different nanotriangle thicknesses with the experimental results. We assumed a solution containing $\sim 10^{12}$ particles consisting of eight different thicknesses. The resulting weighted average spectrum was fitted with a convoluted Cauchy-Lorentz and Gaussian envelope peak. The peculiar blue-shifting and narrowing of the spectrum observed experimentally upon SWCNT conjugation of the Ag nanotriangles was obtained in simulations by tuning the plasma frequency as described above to account for a higher carrier density and using the weighted average coefficients of the eight thicknesses used to model the absorption spectrum of the Ag nanotriangle solution. Notably, by imposing a single charge density shift, this model allowed us to simulate all the experimental observations in the presence of SWCNTs, including the wavelength shift, intensity increase, and peak narrowing. The same method was applied to effectively simulate the behavior of Au nanotriangles, nanorods (Ag and Au) and nanospheres (Ag and Au) in the proximity of SWCNTs. We note that averaged transverse and longitudinal modes were

used in the case of nanorods (Ag and Au) and Au nanotriangles, whereas a single orientation was used for Au and Ag nanospheres because of the particles' spherical symmetry. Therefore, this model accounts for the heterogeneous orientation of the nanoparticles and their variable effects on the enhancement.

3. Results and discussion

Microscopic images of the spherical, rod, and triangular Ag and Au nanostructures, along with their respective absorption spectra, are shown in Fig. 2. The TEM images confirm the distinct nanoparticle geometries for both Ag and Au nanoparticles. The sizes of the nanostructures were measured using TEM and DLS. The Ag and Au nanospheres (Fig. 2a) were synthesized with diameters of 10 nm (Fig. S2). The Au and Ag nanorods have a mean diameter of approximately 6 nm and a mean length of approximately 60 nm (Fig. S3). The Ag and Au nanotriangles (Fig. 2c) have average edge lengths of approximately 20 nm with an average nanoparticle thickness of approximately 8 nm (Fig. S4).

Each of the aforementioned nanoparticles shows distinct absorbance properties that are in agreement with previous reports [59] (Fig. 2, right). The 10 nm Ag and Au nanospheres possess a single-peak dipole plasmon resonance at 400 nm and 520 nm, respectively, while the nanorods show characteristic dipole plasmon resonances (440 and 600 nm for Ag; 540 and 850 nm for Au). The plasmonic modes of the triangular nanostructures are more complex; they exhibit dipole in-plane (600 nm for Ag and 680 nm for Au), dipole out-plane (expected at 500 nm for Ag, which overlaps with the broad 600 nm peak from dipole in-plane and 600 nm for Au), and quadrupole in-plane (350 nm for Ag and 520 nm for Au) plasmon resonances. The absorbance spectrum of ssDNA-SWCNTs shows different peaks in the 300–1400 nm range corresponding to different SWCNT chiralities. The peaks appearing below 550 nm are mainly attributed to metallic nanotubes, whereas peaks in the 600–900 nm and 900–1400 nm ranges are assigned to the E_{22} and E_{11} optical transitions of nanotubes, respectively. The absorbance spectra of the ssDNA-SWCNTs in the presence of the plasmonic nanoparticles are distinct from those of the pristine ssDNA-SWCNTs and those of the nanoparticle solutions. For example, in the presence of Ag nanotriangles, the ssDNA-SWCNTs show an absorbance peak at 475 nm that appears neither in the pristine ssDNA-SWCNT solution nor in the Ag nanotriangle solution. The formation of this peak is consistent with near-field coupling effects. Such near-field effects is expected for ssDNA-SWCNTs as the sub-nm DNA thickness is too thin to account for far-field interactions from the adsorbed nanoparticles, an observation that is consistent with previous work [43]. In addition, a comparison of the semiconducting peaks above 800 nm shows a close overlap in absorbance wavelengths for SWCNTs in the absence and presence of Ag nanotriangles. The alignment of the absorbance spectra, namely the lack of red-shifting and broadening effects at these wavelengths [60–62], indicates the lack of SWCNT aggregation on nanoparticle addition. These measurements therefore confirm the optoelectronic coupling of the nanoparticles with the individual ssDNA-SWCNTs.

Photoluminescence maps of the conjugated nanoparticle-ssDNA-SWCNTs hybrids show that plasmonic enhancement of the NIR-II fluorescence is affected by both nanoparticle composition and shape (Fig. 3) (see Fig. S7 for the quantitative summary of the chirality-specific nanoparticle effect), consistent with the effects of geometric hot spots that can be observed in the near-field. In agreement with the findings of Yang et al. [43], the 10 nm Au nanospheres enhances the (6,5) NIR-II fluorescence, whereas the Ag nanospheres are shown to quench the SWCNT fluorescence (Fig. 3, top row). As depicted in Fig. 2a, the 400 nm Ag absorption

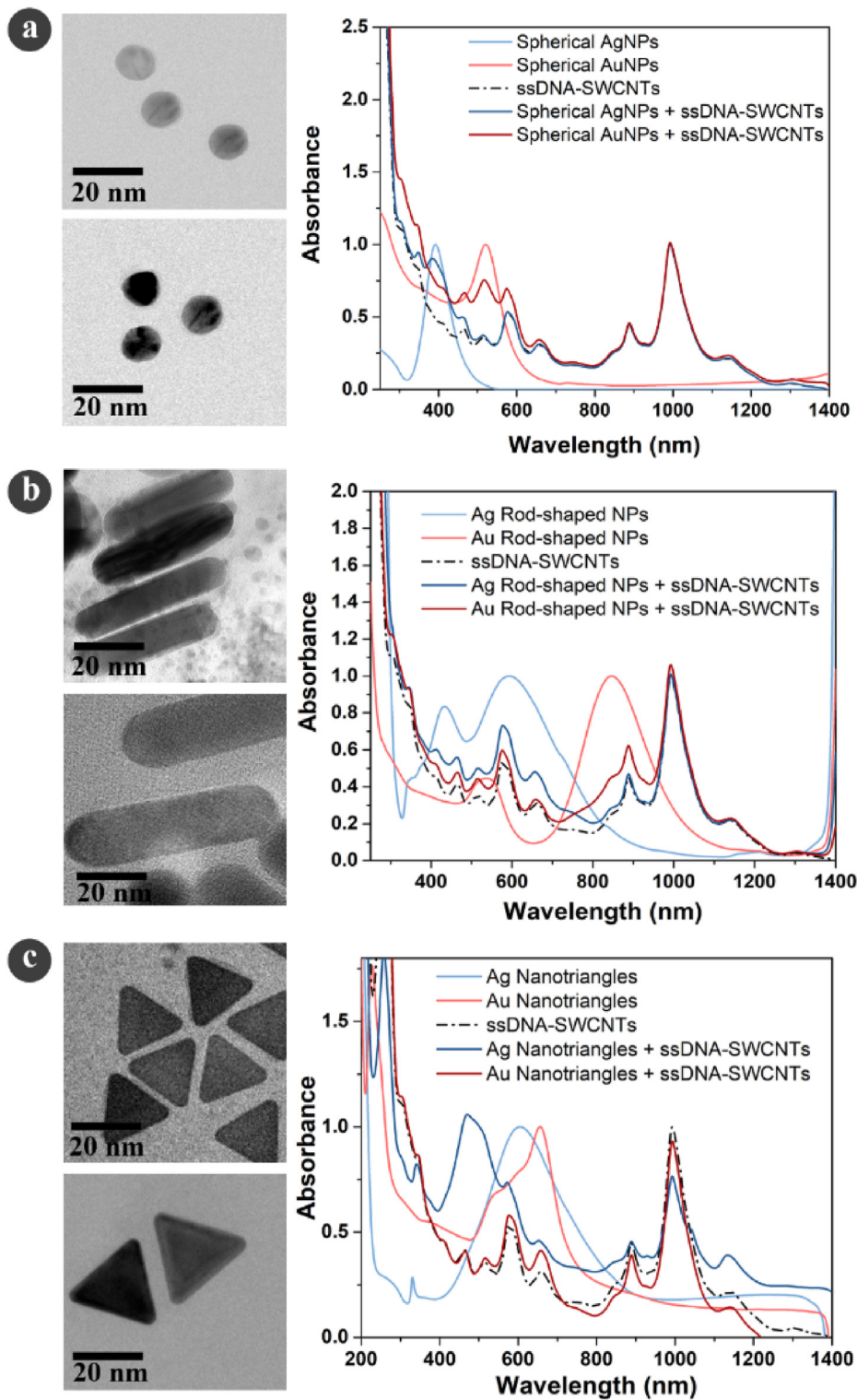


Fig. 2. TEM images and UV–visible absorbance spectra of spherical (a), rod, (b) and triangular (c) nanoparticles. TEM images correspond to Ag (top left) and Au (bottom left) nanoparticles, and the corresponding absorbance spectra (right) are shown for the nanoparticles, pristine ssDNA-SWCNTs, and conjugated ssDNA-SWCNTs with the respective nanoparticles.

peak is blue-shifted relative to the minimum excitation wavelength of the SWCNTs (575 nm for (6,5) chirality), and plasmonic enhancement is not observed in the case of Ag nanospheres. The quenching may therefore be attributed to non-radiative metallic quenching at short distances from the emitter surface [63]. In the

case of Au nanospheres, the fluorescence is enhanced for the (6,5) ssDNA-SWCNTs, whose excitation maximum (575 nm) more closely aligns with the peak absorption of the Au nanoparticle at 520 nm. We note that these findings are in agreement with Yang et al. [43], who similarly reported (6,5) fluorescence enhancement

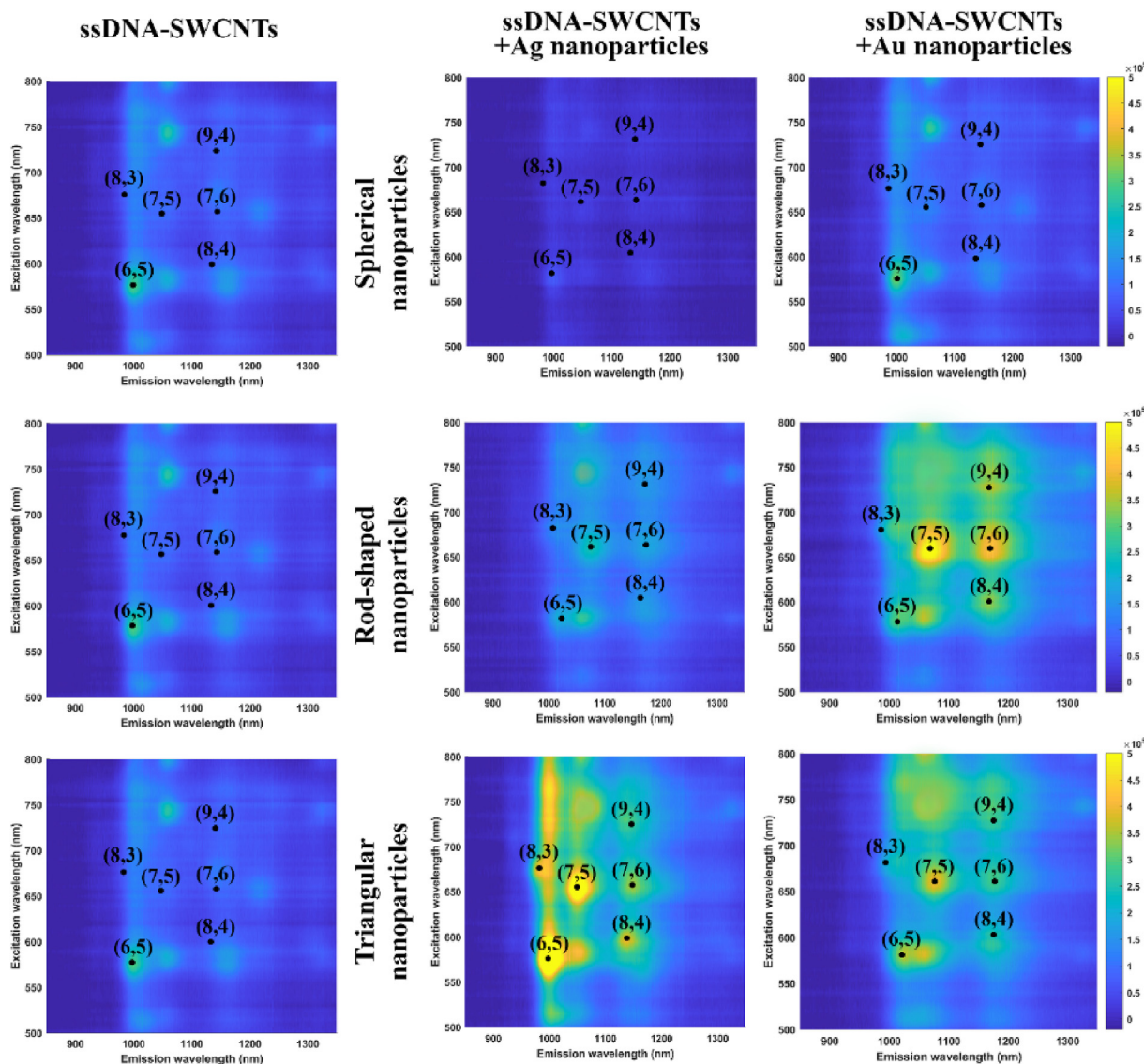


Fig. 3. Excitation–emission maps for ssDNA-SWCNTs conjugated with spherical (top row), rod (middle row), and triangular (bottom row) nanoparticles. Maps are compared between pristine ssDNA-SWCNTs (left column), as well as ssDNA-SWCNTs in the presence of Ag nanoparticles (middle column) and Au nanoparticles (right column).

in the presence of Au nanospheres, as well as previous studies [42,43] that reported enhancements for fluorophores with red-shifted excitation maxima relative to the nanoparticle peak absorption. Negative controls performed in the presence of the nanoparticle capping agents, metal precursors, and reducing agents further support the plasmonic-specific enhancement of the NIR-II fluorescence (Figs. S5 and S6).

Contrary to the nanospheres, both the Ag and Au nanorods were shown to enhance SWCNT fluorescence (Fig. 3, middle row). The Au nanorods, in particular, show an 80% and 50% enhancement of the (7,5) and (7,6) SWCNT chiralities, respectively, which exceed the corresponding 10% and 12% enhancements achieved by the Au nanospheres. The dipole resonance of the nanoparticle at 850 nm is not expected to contribute significantly to the observed plasmonic effects; contributions from absorption peaks that are red-shifted relative to the excitation wavelength are considered negligible [64].

Compared to spherical and rod nanoparticles, the strongest fluorescence enhancement was achieved with triangular Ag nanoparticles (Fig. 3, bottom row). These nanoparticles show a general enhancement across the (6,5), (7,5), (8,3), (8,4), (7,6), and

(9,4) chiralities. The greatest enhancement was observed for the (6,5) chirality, which demonstrates a 240% increase in fluorescence that is over 10 times greater than the less pronounced enhancement achieved with Au nanospheres used in previous studies [43]. Given the dominant role of the (6,5) chirality for nanotube separation and single-chirality sensing applications, the preferential enhancement with the Ag nanotriangles of this chirality poses significant advantages in the field. Interestingly, although the Au nanotriangles showed more modest enhancements compared to the Ag nanotriangles, the fluorescence increase readily surpassed those of the nanospheres despite the lower absorbance. In addition, the shape-dependence of this enhancement, which shows greater enhancements for geometries with pointed, strong localized field effects such as triangles, is in agreement with the predictions of Glaeske et al. [64], who verified plasmonic coupling through time-dependent relaxation measurements. The results are also in agreement with previous reports of chirality-specific enhancement of the plasmonic effects [43]; however, in this case, the chirality specificity can be tuned by engineering the nanoparticle shape and composition. Together, these observations indicate that the

fluorescence enhancement is due to plasmonic coupling effects rather than a mere increase in absorption.

The plasmonically-induced fluorescence enhancement observed in this study can thus be attributed to either (i) increased pumping of the excited electrons from the ground level (S_0) to the S_k ($k > 1$) level and/or (ii) a fast de-excitation of the S_1 excited electrons to the ground level (S_0) [65,66]. Though previous studies have confirmed increased relaxation times for the plasmonically coupled SWCNTs, the enhancement has been primarily attributed to the increased pumping of the excited electrons [64]. The overall enhancement factor (Q) can be written as shown in Equation (6):

$$Q = \frac{|E_m|^2 \cdot \gamma_{\text{rad}} + \gamma_{\text{non-rad}} + \gamma_{\text{metal}}}{|E_0|^2 \cdot \gamma_{\text{rad}} + \gamma_{\text{non-rad}}} \quad (\text{Eq. 6})$$

where the E_0 is the intrinsic excitation rate of the emitter, E_m is the excitation rate in the presence of plasmonic nanoparticles, and γ_{rad} , $\gamma_{\text{non-rad}}$, and γ_{metal} correspond to the rates of the radiative, non-radiative, and metal-induced de-excitation pathways, respectively. The latter de-excitation pathway is specific to phenomena that are only observed in the presence of a metallic surface near the emitter [64]. Though previous reports were unable to elucidate the underlying mechanism for the increased pumping and fast de-excitation of electrons [64], our results similarly indicate that the hybridization of the SWCNTs with plasmonic nanoparticles results in an increase in the charge density. In this study, however, we demonstrate that the extent and chirality specificity of this enhancement is highly dependent on the morphology of the nanostructures. This dependency is attributed to the formation of an electron hotspot near a plasmonic nanoparticle.

To test this hypothesis, we modeled the system using classical electromagnetics with FEM. As described in the Methods section, we assumed an altered electron density for nanoparticle-SWCNT conjugates by modifying the dielectric properties of the Ag nanotriangles [67,68], and the effects of nanoparticle coupling were considered negligible for the low nM concentrations used in this study [69,70]. The broad absorbance peak observed for the Ag nanotriangles (Fig. 2c, blue) illustrates a distribution of various modes of Ag nanotriangles with different thicknesses. Fig. S9 shows the calculated plasmon modes of Ag nanotriangles for eight different thicknesses with and without SWCNTs. The absorbance blue-shift is shown to decrease exponentially with increasing thickness. The predicted absorption peaks of the Ag nanotriangles of various thicknesses (Fig. 4a, light blue) were weighted to fit the observed absorbance spectrum (Fig. 4a, dark blue). The same distribution of nanoparticle thicknesses was assumed when modeling the absorption spectrum of the nanoparticle-SWCNT conjugates (Fig. 4a, purple). The higher carrier density of Ag nanotriangles in our numerical model therefore results in the blue-shifting, narrowing, and increase of the absorption peak, as experimentally observed in Fig. 4b.

As shown in Fig. S10, while the absorption cross-section decreases with decreasing thickness, the electric field enhancement $|E/E_0|^2$ increases with thickness. This enhancement therefore becomes more pronounced when the field is confined to a smaller area [71–73], especially in the vicinity of the plasmonic hot spot. These observations are in agreement with the predictions of Glaeske et al. [64] for plasmonically coupled systems. These larger field enhancements could exert a higher attractive force towards the polarizable nanotube surface, leading to increased SWCNT accumulation and a greater change in carrier density [74–76]. In contrast, the lack of field hotspots for the spherical and rod nanostructures under these conditions would lead to relatively modest changes in the absorbance spectra, in agreement with our experimental observations. Whereas the Ag nanotriangles show more

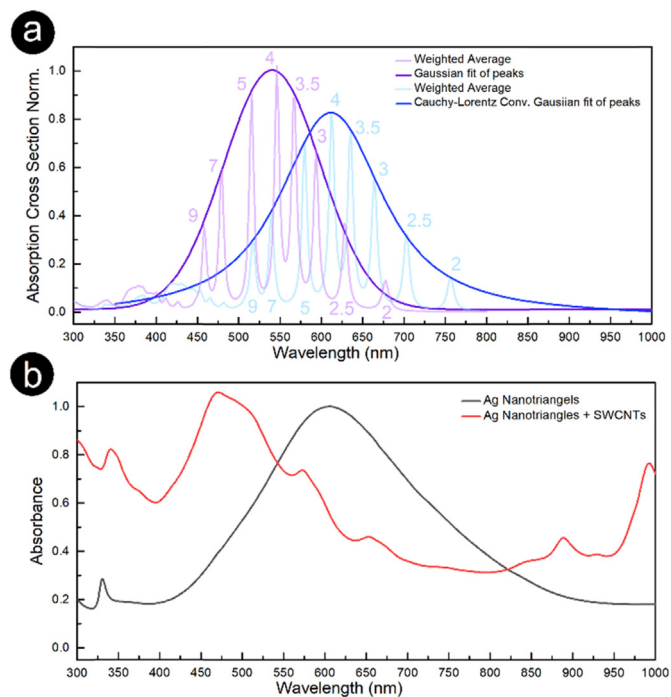


Fig. 4. Comparison of simulated and experimental absorption spectra. (a) Numerical modeling of optical properties of Ag nanotriangles before (blue curve) and after (purple curve) conjugation with SWCNTs. The numbers above each peak correspond to the modeled thicknesses of nanotriangles in nm. (b) Experimentally obtained absorbance spectra of Ag nanotriangles before (black curve) and after (red curve) conjugation with SWCNTs. (A colour version of this figure can be viewed online.)

than a 200-fold enhancement in the local field, the Ag nanorods, Au nanorods, and Ag nanospheres only show a 60-fold, 18-fold, and 12-fold enhancement, respectively. We also note this effect to be material dependent, since such regions with increased charged densities (i.e. blue-shift of the resonance modes) were not observed for the Au nanotriangles (Fig. 2c). The dielectric function of the material can indeed be responsible for the observed difference between Ag and Au (e.g. both the imaginary (ϵ_i) and real (ϵ_r) parts of Ag's dielectric function are lower than those of Au in the studied range) [47]. Therefore, the notable blue-shifting from the Ag nanotriangles is attributed to not only geometric “hot spots” with an enhanced electric field, but also to the lower value of ϵ_r and ϵ_i of the Ag compared to Au.

According to the literature [65,66], the excitation energy ($\gamma_{\text{excitation}}$), or incoupling, of the SWCNTs in the presence of the plasmonic particles can be qualitatively estimated from the local electric field enhancement of the plasmonic hot spots and the optical response of the fluorophore (Equation (7)). The dipole moment of the fluorophore, μ_{Abs} , is directly proportional to the absorbance of the fluorophore (A_{SWCNTs}), the latter of which can be obtained experimentally for the SWCNTs.

$$\gamma_{\text{excitation}} \propto |\mu_{\text{Abs}} E|^2 \cdot \alpha A_{\text{SWCNTs}}^2 |E|^2 \quad (\text{Eq. 7})$$

The emission wavelength intensity (γ_{emission}), or outcoupling, of the SWCNT is determined by the local density of optical states (LDOS), which is altered in the presence of the plasmonic particles. If we assume the LDOS to be characteristic of the absorbance spectrum of the system containing the coupled SWCNTs and plasmonic nanoparticles ($A_{\text{SWCNT} + \text{NP}}$), we arrive at the following relation:

$$\gamma_{\text{emission}} \propto \text{LDOS} \propto A_{\text{SWCNT}+\text{NP}} \quad (\text{Eq. 8})$$

Orthogonal vector multiplication between the excitation rate of the fluorophore (Equation (7)) and the LDOS (Equation (8)) yield the following two-dimensional spectrogram for numerically approximating the fluorescence enhancement (FE):

$$FE = \gamma_{\text{excitation}} \times \gamma_{\text{emission}} \quad (\text{Eq. 9})$$

Therefore, the field enhancement modeled by Equations (7)–(9) takes into consideration the incoupling effects, as determined by the altered dipole moment of the fluorophore, as well as the out-coupling effects arising from the modified LDOS. If we define the experimentally measured excitation-emission map for the bare ssDNA-SWCNTs as $PL_{\text{ssDNA-SWCNT}}$, then the numerically simulated fluorescence (NF) can be modeled according to Equation (10):

$$NF = FE \times PL_{\text{ssDNA-SWCNT}} \quad (\text{Eq. 10})$$

As shown in the NF plots in Fig. 5, minimal fluorescence

enhancement is predicted for the Ag nanospheres and Au nanospheres, and the greatest enhancement is predicted for the Ag nanotriangles, followed by the Au nanorods and Au nanotriangles. These predictions are in agreement with the experimental observations shown in Fig. 3 (see Fig. S17 for comparison of experimental and simulated plots). The Ag nanospheres in particular show the least enhancement, as their absorption peak lies outside the studied excitation range (500–800 nm) (Fig. S11).

Despite the overall agreement of the predicted trends with our experimental observations, we note several key differences. For example, the metallic quenching effects experimentally observed for the Ag nanospheres in Fig. 3 are not modeled in this system, and the perceived quenching shown in Fig. 5 is due to normalization of the plot relative to the enhanced intensity that is predicted for the (6,5) nanotube. In addition, the predicted model underestimates the fluorescence enhancement that is observed experimentally for the (7,5) nanotube. Since the experimentally measured (7,5) ssDNA-SWCNT is minimal (Fig. 5, left), this enhancement is attributed to plasmonic effects beyond the altered electron density contributions

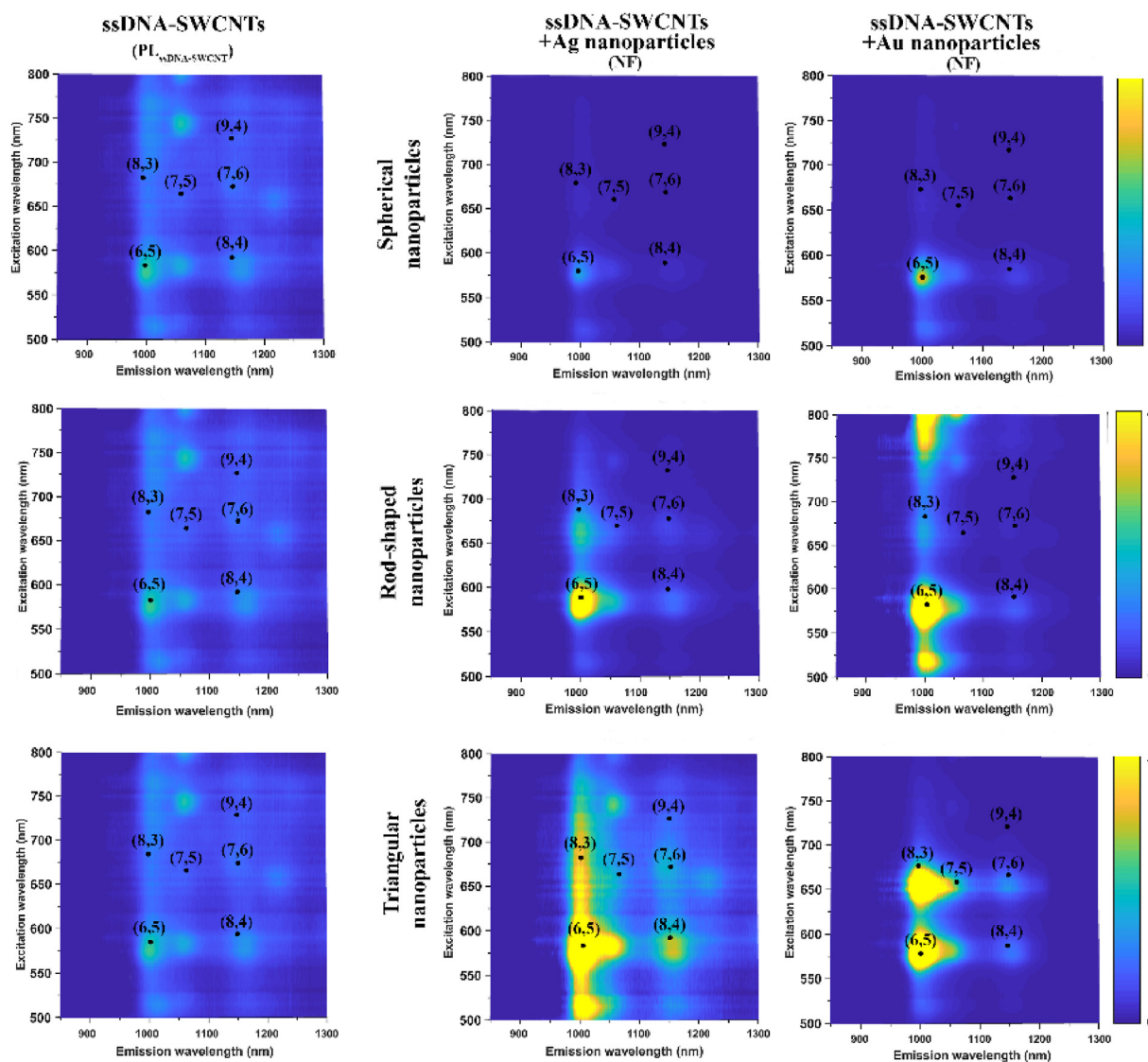


Fig. 5. Predicted excitation-emission maps for ssDNA-wrapped SWCNTs in the presence of Ag and Au nanoparticles. Each map was normalized by the maximum value for each nanoparticle-SWCNT system in order to avoid saturation. $PL_{\text{ssDNA-SWCNT}}$ and NF refer to experimentally measured excitation-emissions map for ssDNA-SWCNTs and the numerically simulated fluorescence of the ssDNA-SWCNTs in the presence of nanoparticles, respectively.

modeled herein. Indeed, Takase and co-workers observed the breakdown of electronic wave function selection rules in the presence of strong electromagnetic fields, such as those generated by plasmonic effects [77]. This breakdown yields altered optoelectronic signatures resulting from forbidden and dark exciton transitions that become enabled on excitation in the radial direction of the nanotube. Amori et al. [78] further reported enhanced photoluminescence resulting from dark exciton formation of the (7,5) chirality. Since the enhancement observed in this study occurs at the resonant (7,5) E_{22} excitation and E_{11} emission wavelengths, E_{22} excitation of a dark exciton state may ultimately non-radiatively decay to the E_{11} state prior to radiative recombination. This proposed mechanism is supported by fluorescence emissions spectra taken at 633 nm excitation (Fig. S18), which shows a weak peak at 1185 nm (~130 meV) that is not assigned to any residual fluorescence emission from other chiralities. This peak, which is most pronounced for the Au nanorods and Au nanotriangles, is in close agreement with the photoluminescence feature for the K-momentum dark state of the (7,5) chirality that has been previously observed and characterized by Amori et al. [78]. In also considering the short lifetime of the exciton (<100 fs) [79,80], which suggests relaxation to the E_{11} state to be favored over alternative scattering-based recombination pathways, the photoluminescence data therefore indicate contributions from the activation of dark excitons. These observations support our hypothesis that the deviation observed for the (7,5) may be accounted for by photophysical phenomena beyond those modeled in our simulations.

To test this hypothesis, we extended the method presented above to account for the altered absorption spectrum of the SWCNTs in the presence of the Ag nanotriangles. Specifically, we subtracted the absorption spectrum of the Ag nanotriangles from that of the ssDNA-SWCNTs in the presence of Ag nanotriangles to obtain the altered SWCNT absorption spectrum shown in Fig. S15. This modified absorption spectrum can be used to calculate the efficiency of the E_{22} to E_{11} relaxation pathway, γ , according to the relation [81]:

$$\gamma = \left[\frac{\int E_{22}(\text{PLE})}{\int E_{11}(\text{PLE})} \right] \times \left[\frac{\int E_{22}(\text{abs})}{\int E_{11}(\text{abs})} \right] \quad (\text{Eq. 11})$$

where $\int E_{ii}(\text{PLE})$ and $\int E_{ii}(\text{ABS})$ represent the integrated areas of the fluorescence and absorption peaks for the corresponding ii transitions, respectively. As shown in the figure, we observe a relative decrease in the E_{22} absorption peak of the (7,5) chirality that is expected to contribute to an overall increase in the efficiency of excitons that undergo E_{22} to E_{11} radiative decay as opposed to excitations lost to mechanisms such as scattering. Indeed, as shown in Fig. S16, the NF calculated from this altered absorption spectrum is able to capture enhanced fluorescence emissions across longer wavelengths, including those of the (7,5) chirality, that are observed experimentally. However, we note that this plot consequently underestimates the observed enhancements across longer excitation wavelengths compared to the NF plots based on the unaltered ssDNA-SWCNT fluorescence in Fig. 3.

In addition to nanoparticle material and shape, plasmonic effects have also been shown to vary with nanoparticle distance [82–84] and salt concentration [85]. According to the proposed enhancement mechanism, the SWCNTs must remain in the vicinity (up to 10 nm) of the plasmonic nanostructures to achieve the enhanced field effects [84]. To investigate this effect, the distance between the plasmonic nanoparticle and SWCNT was varied by coating the nanoparticle surface with PVP, a neutral steric spacer (Fig. 6a). Previous studies have shown that the thickness of the PVP

layer increases with PVP concentration due to molecular stacking [86–89]. In agreement with near-field plasmonic theory, we indeed observe a decrease in ssDNA-SWCNT fluorescence with increasing PVP concentration in the presence of Ag nanotriangles (Fig. 6b, excitation-emission plots are provided in Fig. S12). At sufficiently high concentrations of PVP, the fluorescence intensity approaches values that are achieved in the absence of the nanoparticles. These observations are consistent with previous studies that have reported decreasing plasmonic effects with increasing distance from fluorophores, including SWCNTs [15,90]. We further note that no significant fluorescence changes were observed in the absence of the nanoparticles, confirming that the diminution is due to nanoparticle effects.

To verify the plasmonic dependence on salt concentration, we monitored the change in SWCNT fluorescence on increasing NaCl concentrations in the presence of the Ag nanotriangles. As shown in Fig. 6c, we observe a gradual increase, followed by a stark diminution, of fluorescence with increasing NaCl concentrations (excitation-emission plots are provided in Fig. S13). The sharp diminution occurs at NaCl concentrations exceeding 78 mM, which corresponds to the NaCl concentration at which plasmonic nanoparticles have been shown to undergo abrupt wavelength shifting [85]. We note that the initial increase observed at lower NaCl concentrations could be attributed to salt effects on ssDNA-SWCNT fluorescence. In fact, previous studies have reported increases in ssDNA-SWCNT fluorescence with increasing monovalent salt concentrations for certain DNA sequences in the absence of any plasmonic nanoparticles [90,91]. Such fluorescence increases have been attributed to the increase in oxygen exclusion at the nanotube surface due to tighter DNA wrapping. However, no significant changes in fluorescence were observed under the conditions (66–90 mM NaCl range, (AT)₁₅ ssDNA sequence) used in this study. These observations indicate that the fluorescence changes in the presence of the nanoparticle are unlikely to be due to the DNA surface coverage and oxygen exclusion effects reported previously [91,92].

Previous studies have also shown that DNA sequence plays a significant role in both SWCNT surface coverage and fluorescence response [50,93–98]. Consequently, different DNA sequences with altered surface functionalizations are expected to show variable responsivities to plasmonic nanoparticles, whose efficacy depends on SWCNT surface accessibility and distance. To test this hypothesis, SWCNTs were wrapped in A₃₀, C₃₀, and T₃₀, and their fluorescence enhancements were compared in the presence of Ag nanotriangles. As shown in Fig. 6d, whereas the A₃₀, C₃₀, and T₃₀ sequences all showed comparable initial fluorescence intensities under the tested measurement conditions, the fluorescence enhancements vary with ssDNA sequence. These enhancement effects are also distinct from that of the AT₁₅ sequence, which shows a higher initial fluorescence intensity prior to nanoparticle addition, in agreement with previous reports [24]. The plasmonic effect on the G₃₀ sequence was not studied due to the poor suspension quality of the nanotube solution (data not shown).

Finally, we demonstrate the applicability of the enhanced fluorescence emission for single-molecule NIR fluorescence imaging of individual SWCNTs. SWCNT fluorescence is renowned for its strong sensitivity to the nanotube environment. This sensitivity has enabled the optical detection NO, H₂O₂, and most recently, micro-RNA [16,24,99,100] down to the single-molecule level. The sensitivity limits of these single-molecule sensors have been shown to depend on the fluorescence quantum yield [26,101].

Although recent developments in NIR confocal microscopy enable increased single-molecule imaging resolution of individual SWCNTs, the improved resolution occurs at the expense of significant fluorescence losses [51], which further compromise the

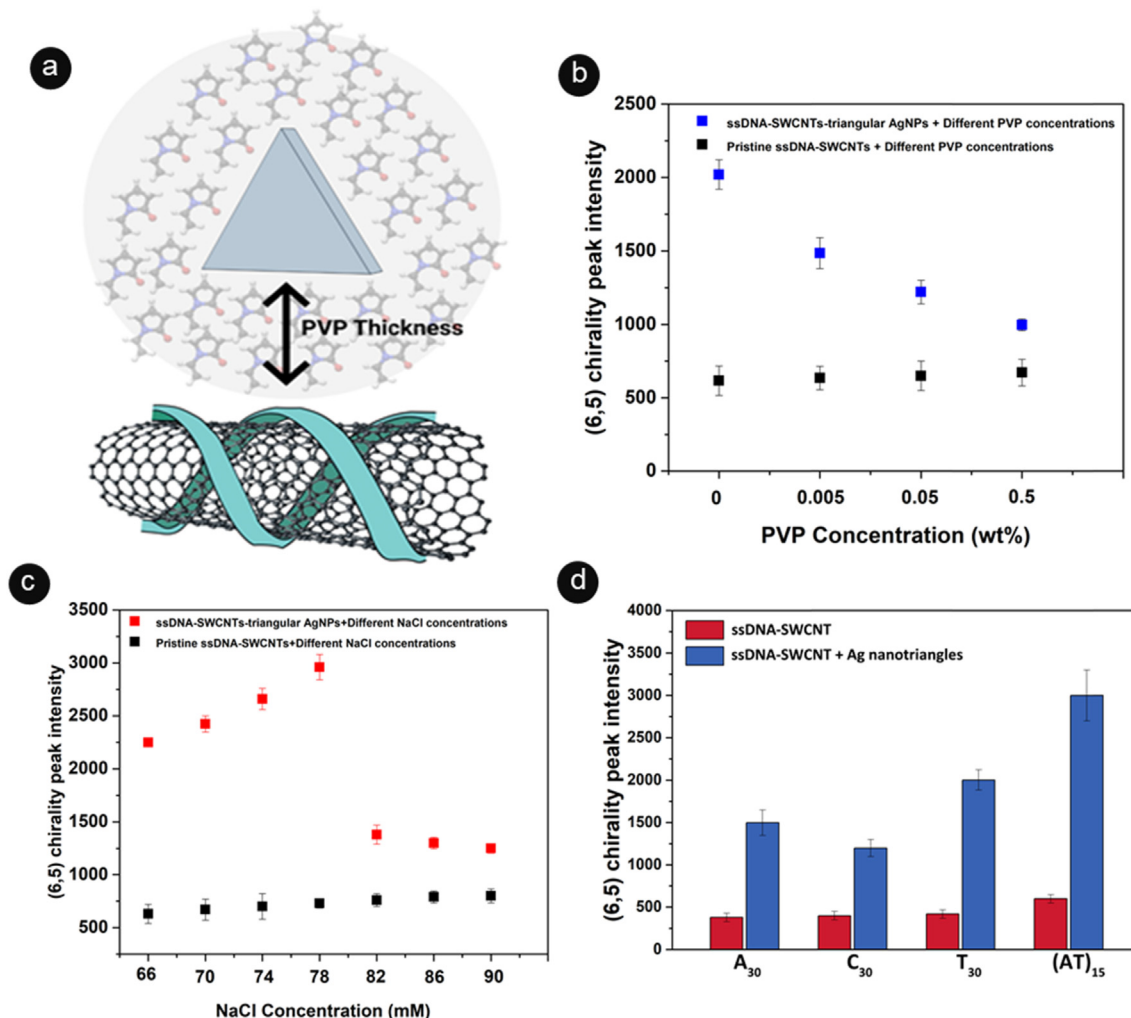


Fig. 6. The effect of nanoparticle distance, salt concentration, and DNA sequence on the photoluminescence of ssDNA-SWCNTs. (a) Schematic representation of the effect of PVP thickness on modulating distance between plasmonic nanoparticles and ssDNA-SWCNTs. (b) Fluorescence intensity of (6,5) ssDNA-SWCNT emission peak in the presence of Ag nanotriangles and varying PVP concentrations (0–0.5 wt% PVP). Control measurements are shown for ssDNA-SWCNTs in the absence of the nanoparticles. (c) Fluorescence intensity of (6,5) ssDNA-SWCNT emission peak in the presence of Ag nanotriangles and varying salt concentrations (66–90 mM NaCl). Control measurements are shown for ssDNA-SWCNTs in the absence of the nanoparticles. (d) Fluorescence intensity of (6,5) ssDNA-SWCNTs suspended with AT₁₅, A₃₀, and T₃₀ sequences in the absence (red) and the presence (blue) of Ag nanotriangles. (A colour version of this figure can be viewed online.)

sensitivity of the nanosensors. However, as shown in the confocal NIR images in Fig. 7a, the ssDNA-SWCNTs conjugates show a significant enhancement in single-molecule imaging in the presence of the Ag nanotriangles. A comparison of the corresponding single-molecule intensities shown in the histograms of Fig. 7b confirms the increase in the intensity of individual, immobilized SWCNTs that are not aggregated.

The confocal single-molecule images were further used to demonstrate the use of the SWCNT conjugates for ferricyanide detection. Previous reports have shown a fluorescence decrease of SWCNTs in the presence of ferricyanide [102]. In agreement with these observations, the average fluorescence intensity of the individual SWCNTs is shown to decrease on ferricyanide addition (Fig. 7c). At high concentrations of ferricyanide (100 mM), the fluorescence quenching effects become saturated for both the plasmonically coupled and non-coupled SWCNTs. Under these saturating conditions, the plasmonically coupled and non-coupled SWCNTs converge to the same average final intensity, with the plasmonically coupled SWCNTs demonstrating over a two-fold reduction in the overall fluorescence intensity compared to the

non-coupled SWCNTs. At lower concentrations of ferricyanide, the plasmonically coupled SWCNTs show a concentration-dependent response to increasing concentrations of ferricyanide. By contrast, the bare ssDNA-SWCNTs show little to no concentration dependence, reaching a saturated response at concentrations as low as 0.1 mM. The increased sensitivity of the plasmonically enhanced SWCNTs across analyte concentrations spanning four orders of magnitude thus motivates their use for sensing.

4. Conclusions and outlook

Metallic nanoparticles offer a tunable approach to modulating SWCNT NIR fluorescence. By altering the nanoparticle material and shape, these nanoparticles can be engineered to tune the fluorescence of different nanotube chiralities to varying extents. Based on the FEM results, the chirality-specific fluorescence increase can be at least partially attributed to a combination of localized near-field enhancements from geometric “hot spots”, as well as the dielectric properties of the material. These findings are in agreement with plasmon theory, which predicts a geometric and material

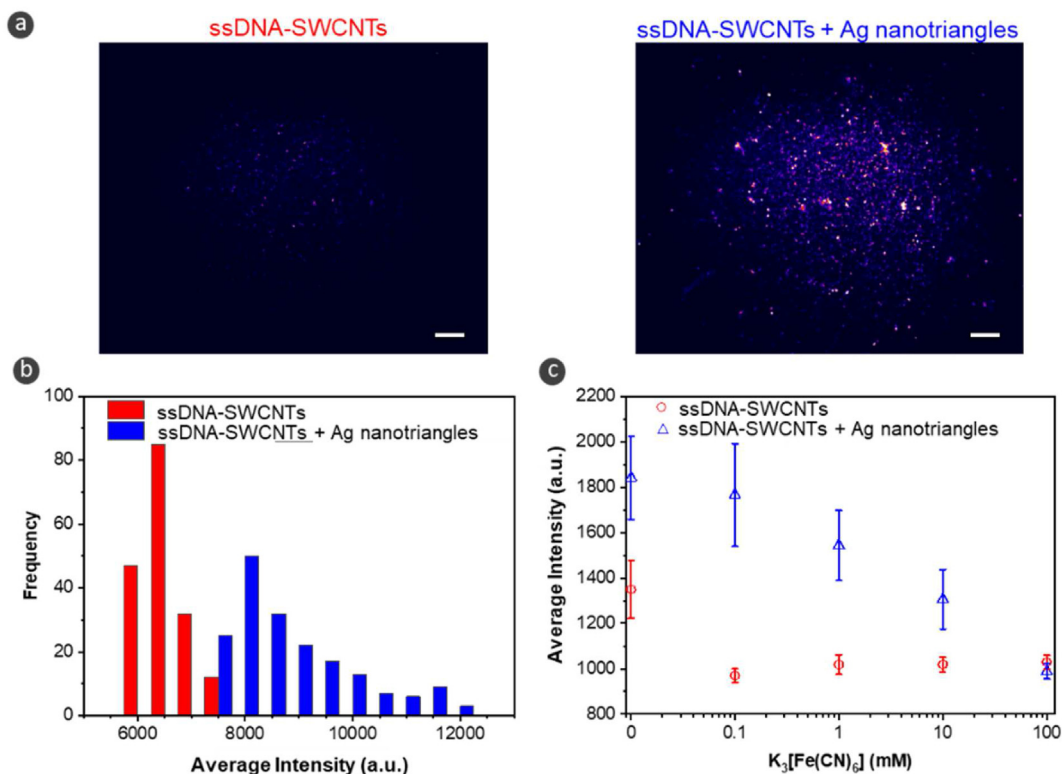


Fig. 7. Single-molecule confocal NIR photoluminescence imaging of ssDNA-SWCNTs. (a) Fluorescence images of ssDNA-SWCNTs on a glass substrate before (left) and after (right) hybridization with Ag nanotriangles. Scale bars are 10 μ m. (b) Histograms showing frequency distributions of photoluminescence intensities of individual SWCNTs in the presence and absence of Ag nanotriangles. (c) Average photoluminescence intensities of individual SWCNTs in the presence and absence of Ag nanotriangles with increasing concentrations of ferricyanide. Error bars represent ± 1 S.D. In all images, samples were excited at 640 nm, and emission was collected above 980 nm using a long-pass filter. The 200 brightest 2×2 pixelated regions were considered for the histograms and data points shown in (b) and (c), respectively.

dependence. The theory also predicts a plasmonic dependence on nanoparticle size [46,103,104]. Although the effects of nanoparticle size were not experimentally studied in this work, the FEM results presented herein were able to capture the effects of altering nanotriangle thickness, which is shown to affect the absorbance and, consequently, the plasmonic behavior of the system. This size dependence therefore offers an additional avenue for further tuning the SWCNT NIR fluorescence.

In addition to size, material, and shape, the SWCNT fluorescence has also been shown to vary with nanoparticle distance, salt concentration, and DNA wrapping sequence. Whereas the dependence on nanoparticle distance and salt concentration is in agreement with previous observations from other nanoparticle-fluorophore systems [15,86,90], the plasmonic modulation of SWCNT fluorescence with DNA sequence has yet to be reported. Indeed, the DNA sequence space offers a vast range of possibilities for fine-tuning parameters such as nanoparticle distance and nanotube surface exposure in a readily scalable and high-throughput manner. Although the understanding between DNA sequence and surface coverage is lacking and efforts to engineer DNA sequences with desired photophysical effects remain largely empirical, new techniques are being developed to design sequences in a more guided manner [97,105]. In addition to DNA design, advancements in SWCNT chirality separation [106] offers a promising avenue for more precisely controlling the donor-emitter distances in these non-covalent SWCNT-nanoparticle conjugates. The distribution of SWCNT chiralities in the mixture used in this study yields a distribution of DNA coverage, even when the mixture is solubilized with a single DNA sequence. This distribution results in an inherent variability in the distances between the ssDNA-SWCNT and

adsorbed nanoparticles. The various distances and chiralities limit the applicability of time-resolved and other analyses that require precise control over donor-emitter separation. The ability to purify single-chirality SWCNTs would thus enable additional studies that would allow one to more precisely modulate near-field and far-field effects by more uniformly controlling the donor-emitter distances.

In addition to the experimental agreement with predicted trends, the plasmonic effects were also captured using FEM. The modeling results confirm the plasmonic effects on SWCNT fluorescence. Importantly, they also represent a first-of-its-kind modeling demonstration of a complex system containing a mixture of NIR fluorophores with distinct bandgaps and excitation-emission properties. The FEM of such complex systems allows one to capture the resonance conditions of a given plasmonic nanoparticle by screening the fluorescence effects of different bandgap fluorophores. Indeed, this ability is exemplified by the chirality-dependent differences that were modeled and experimentally confirmed for each of the distinct nanoparticles. The limitations in the model predictions, which include omission of quenching effects due to metal contact and the underestimation of the (7,5) fluorescence enhancement, further point to additional photophysical contributions beyond conventional plasmonic effects. The underestimation of the (7,5) fluorescence, in particular, suggests radiative decay of otherwise forbidden transitions and dark states. This hypothesis is supported by previous studies that have reported the breakdown of the radiative SWCNT selection rules in the presence of a strong field and the observed fluorescence peak 130 meV at 633 nm excitation. While the population and de-population of dark states remain an area of active research [107–109], the model presented herein provides one avenue for studying such quantum

phenomena in the presence of a plasmonic field.

From an applications perspective, the fluorescence enhancement from these plasmonic nanoparticles is especially beneficial for NIR sensing and imaging. In particular, we demonstrate the single-molecule, confocal NIR imaging of SWCNTs, which has yet to be reported in the literature. Whereas such imaging applications are conventionally hindered by low QYs and significant microscope fluorescence losses, we are able to overcome such challenges through nanoparticle coupling. Through nanoparticle coupling, we show up to a 240% enhancement in fluorescence emissions and increased responsivity of a single-molecule sensor using confocal microscopy. This demonstration represents just one of many SWCNT applications that readily benefit from the enhanced fluorescence demonstrated herein.

Declaration of competing interest

The authors declare that they have no known competing financial interests or personal relationships that could have appeared to influence the work reported in this paper.

Acknowledgments

The authors are thankful for support from the Swiss National Science Foundation Assistant Professor (AP) Energy Grant (Project No. PYAPP2_154269) and Swiss National Science Foundation Project No. 200021_184822. T.V. Tsoulos acknowledges the SNSF Spark Grant #CRSK-2_190809. G.T acknowledges the SNSF Eccellenza Grant #PCEGP2_194181.

Appendix A. Supplementary data

Supplementary data to this article can be found online at <https://doi.org/10.1016/j.carbon.2022.03.040>.

References

- [1] N.C. Panoui, W.E.I. Sha, D.Y. Lei, G.C. Li, Nonlinear optics in plasmonic nanostructures, *J. Opt.* 20 (2018), 083001, <https://doi.org/10.1088/2040-8986/aac8ed>.
- [2] M.B. Ross, C.A. Mirkin, G.C. Schatz, Optical properties of one-, two-, and three-dimensional arrays of plasmonic nanostructures, *J. Phys. Chem. C* 120 (2016) 816–830, <https://doi.org/10.1021/acs.jpcc.5b10800>.
- [3] L. Shao, M. Käll, Light-driven rotation of plasmonic nanomotors, *Adv. Funct. Mater.* 28 (2018) 1706272, <https://doi.org/10.1002/adfm.201706272>.
- [4] J. Zhao, Y. Cheng, H. Shen, Y.Y. Hui, T. Wen, H.C. Chang, et al., Light emission from plasmonic nanostructures enhanced with fluorescent nanodiamonds, *Sci. Rep.* 8 (2018) 1–8, <https://doi.org/10.1038/s41598-018-22019-z>.
- [5] J.A. Schuller, E.S. Barnard, W. Cai, Y.C. Jun, J.S. White, M.L. Brongersma, Plasmonics for extreme light concentration and manipulation, *Nat. Mater.* 9 (2010) 193–204, <https://doi.org/10.1038/nmat2630>.
- [6] A. Comin, L. Manna, New materials for tunable plasmonic colloidal nanocrystals, *Chem. Soc. Rev.* 43 (2014) 3957–3975, <https://doi.org/10.1039/c3cs60265f>.
- [7] J.B. Lassiter, H. Sobhani, J.A. Fan, J. Kundu, F. Capasso, P. Nordlander, et al., Fano resonances in plasmonic nanoclusters: geometrical and chemical tunability, *Nano Lett* 10 (2010) 3184–3189, <https://doi.org/10.1021/nl102108u>.
- [8] C.F. Chen, S. Der Tzeng, H.Y. Chen, K.J. Lin, S. Gwo, Tunable plasmonic response from alkanethiolate-stabilized gold nanoparticle superlattices: evidence of near-field coupling, *J. Am. Chem. Soc.* 130 (2008) 824–826, <https://doi.org/10.1021/ja0773610>.
- [9] R. Bukasov, J.S. Shumaker-Parry, Silver nanocrescents with infrared plasmonic properties as tunable substrates for surface enhanced infrared absorption spectroscopy, *Anal. Chem.* 81 (2009) 4531–4535, <https://doi.org/10.1021/ac900477p>.
- [10] J. Dong, Z. Zhang, H. Zheng, M. Sun, Recent progress on plasmon-enhanced fluorescence, *Nanophotonics* 4 (2015) 472–490, <https://doi.org/10.1515/nanoph-2015-0028>.
- [11] C.Y. Li, M. Meng, S.C. Huang, L. Li, S.R. Huang, S. Chen, et al., Smart Ag nanostructures for plasmon-enhanced spectroscopies, *J. Am. Chem. Soc.* 137 (2015) 13784–13787, <https://doi.org/10.1021/jacs.5b09682>.
- [12] H. Yuan, Y. Lu, Z. Wang, Z. Ren, Y. Wang, S. Zhang, et al., Single nanoporous gold nanowire as a tunable one-dimensional platform for plasmon-enhanced fluorescence, *Chem. Commun.* 52 (2016) 1808–1811, <https://doi.org/10.1039/c5cc08149a>.
- [13] M. Wang, G. Hartmann, Z. Wu, L. Scarabelli, B.B. Rajeeva, J.W. Jarrett, et al., Controlling plasmon-enhanced fluorescence via intersystem crossing in photoswitchable molecules, *Small* 13 (2017) 1701763, <https://doi.org/10.1002/smll.201701763>.
- [14] Y. Fu, J. Zhang, J.R. Lakowicz, Plasmon-enhanced fluorescence from single fluorophores end-linked to gold nanorods, *J. Am. Chem. Soc.* 132 (2010) 5540–5541, <https://doi.org/10.1021/ja1087997>.
- [15] G. Hong, S.M. Tabakman, K. Welscher, H. Wang, X. Wang, H. Dai, Metal-enhanced fluorescence of carbon nanotubes, *J. Am. Chem. Soc.* 132 (2010) 15920–15923, <https://doi.org/10.1021/ja1087997>.
- [16] J.D. Harvey, H.A. Baker, M.V. Ortiz, A. Kentsis, D.A. Heller, HIV detection via a carbon nanotube RNA sensor, *ACS Sens.* 4 (2019) 1236–1244, <https://doi.org/10.1021/acssensors.9b00025>.
- [17] N. Danné, A.G. Godin, Z. Gao, J.A. Varela, L. Groc, B. Lounis, et al., Comparative analysis of photoluminescence and upconversion emission from individual carbon nanotubes for bioimaging applications, *ACS Photonics* 5 (2018) 359–364, <https://doi.org/10.1021/acsp Photonics.7b01311>.
- [18] N.M. Iverson, G. Bisker, E. Farias, V. Ivanov, J. Ahn, G.N. Wogan, et al., Quantitative tissue spectroscopy of near infrared fluorescent nanosensor implants, *J. Biomed. Nanotechnol.* 12 (2016) 1035–1047, <https://doi.org/10.1166/jbn.2016.2237>.
- [19] F. Yang, X. Wang, D. Zhang, J. Yang, D. Luo, Z. Xu, et al., Chirality-specific growth of single-walled carbon nanotubes on solid alloy catalysts, *Nature* 510 (2014) 522–524, <https://doi.org/10.1038/nature13434>.
- [20] A.L. Antaris, O.K. Yaghi, G. Hong, S. Diao, B. Zhang, J. Yang, et al., Single chirality (6,4) single-walled carbon nanotubes for fluorescence imaging with silicon detectors, *Small* 11 (2015) 6325–6330, <https://doi.org/10.1002/sml.201501530>.
- [21] J. Pan, F. Li, J.H. Choi, Single-walled carbon nanotubes as optical probes for bio-sensing and imaging, *J. Mater. Chem. B* 5 (2017) 6511–6522, <https://doi.org/10.1039/c7tb00748e>.
- [22] H. Yi, D. Ghosh, M.H. Ham, J. Qi, P.W. Barone, M.S. Strano, et al., M13 phage-functionalized single-walled carbon nanotubes as nanopores for second near-infrared window fluorescence imaging of targeted tumors, *Nano Lett* 12 (2012) 1176–1183, <https://doi.org/10.1021/nl2031663>.
- [23] M.A. Lee, F.T. Nguyen, K. Scott, N.Y.L. Chan, N.A. Bakh, K.K. Jones, et al., Implanted nanosensors in marine organisms for physiological biollogging: design, feasibility, and species variability, *ACS Sens.* 4 (2019) 32–43, <https://doi.org/10.1021/acssensors.8b00538>.
- [24] J. Zhang, A.A. Boghossian, P.W. Barone, A. Rwei, J.H. Kim, D. Lin, et al., Single molecule detection of nitric oxide enabled by d(AT)15 DNA adsorbed to near infrared fluorescent single-walled carbon nanotubes, *J. Am. Chem. Soc.* 133 (2011) 567–581, <https://doi.org/10.1021/ja1084942>.
- [25] T. Sakashita, Y. Miyauchi, K. Matsuda, Y. Kanemitsu, Plasmon-assisted photoluminescence enhancement of single-walled carbon nanotubes on metal surfaces, *Appl. Phys. Lett.* 97 (2010), 063110, <https://doi.org/10.1063/1.3467834>.
- [26] A.J. Lee, X. Wang, L.J. Carlson, J.A. Smyder, B. Loesch, X. Tu, et al., Bright fluorescence from individual single-walled carbon nanotubes, *Nano Lett* 11 (2011) 1636–1640, <https://doi.org/10.1021/nl200077t>.
- [27] F. Sen, A.A. Boghossian, S. Sen, Z.W. Ulissi, J. Zhang, M.S. Strano, Observation of oscillatory surface reactions of riboflavin, trolox, and singlet oxygen using single carbon nanotube fluorescence spectroscopy, *ACS Nano* 6 (2012) 10632–10645, <https://doi.org/10.1021/nn303716n>.
- [28] X. Wu, M. Kim, H. Kwon, Y. Wang, Photochemical creation of fluorescent quantum defects in semiconducting carbon nanotube hosts, *Angew. Chem.* 130 (2018) 656–661, <https://doi.org/10.1002/ange.201709626>.
- [29] H. Onitsuka, T. Fujigaya, N. Nakashima, T. Shiraki, Control of the near infrared photoluminescence of locally functionalized single-walled carbon nanotubes via doping by azacrown-ether modification, *Chem. Eur. J.* 24 (2018) 9393–9398, <https://doi.org/10.1002/chem.201800904>.
- [30] X. Ma, H. Htoon, Tailoring the photophysical properties of carbon nanotubes by photonic nanostructures, *Mod. Phys. Lett. B* 29 (2015), <https://doi.org/10.1142/S0217984915300045>.
- [31] A. Wroblewska, G. Gordeev, A. Duzynska, S. Reich, M. Zdrojek, Doping and plasmonic Raman enhancement in hybrid single walled carbon nanotubes films with embedded gold nanoparticles, *Carbon N. Y.* 179 (2021) 531–540, <https://doi.org/10.1016/j.carbon.2021.04.079>.
- [32] O. Pavelka, S. Dyakov, J. Veselý, A. Fučíková, H. Sugimoto, M. Fujii, et al., Optimizing plasmon enhanced luminescence in silicon nanocrystals by gold nanorods, *Nanoscale* 13 (2021) 5045–5057, <https://doi.org/10.1039/d1nr00058f>.
- [33] A.A. Sergeev, D.V. Pavlov, A.A. Kuchmizhak, M.V. Lapine, W.K. Yiu, Y. Dong, et al., Tailoring spontaneous infrared emission of HgTe quantum dots with laser-printed plasmonic arrays, *Light Sci. Appl.* 9 (2020) 2047–7538, <https://doi.org/10.1038/s41377-020-0247-6>.
- [34] Y. Omura, Y. Matsubayashi, T. Kishimoto, S.N. Kudoh, C. Hosokawa, K. Tawa, Two-photon-excited emission of quantum dots with a plasmonic chip, *J. Phys. Chem. C* 124 (2020) 16076–16082, <https://doi.org/10.1021/acs.jpcc.0c00826>.
- [35] R. Lv, F. Yang, X. Jiang, B. Hu, X. Zhang, X. Chen, et al., Plasmonic modulated upconversion fluorescence by adjustable distributed gold nanoparticles,

- J. Lumin. 220 (2020) 116974, <https://doi.org/10.1016/j.jlumin.2019.116974>.
- [36] M. Scolari, A. Mews, N. Fu, A. Myalitsin, T. Assmus, K. Balasubramanian, et al., Surface enhanced Raman scattering of carbon nanotubes decorated by individual fluorescent gold particles, *J. Phys. Chem. C* 112 (2008) 391–396, <https://doi.org/10.1021/jp076190i>.
- [37] X. Wang, C. Wang, L. Cheng, S.T. Lee, Z. Liu, Noble metal coated single-walled carbon nanotubes for applications in surface enhanced Raman scattering imaging and photothermal therapy, *J. Am. Chem. Soc.* 134 (2012) 7414–7422, <https://doi.org/10.1021/ja300140c>.
- [38] Y.C. Chen, R.J. Young, J.V. Macpherson, N.R. Wilson, Single-walled carbon nanotube networks decorated with silver nanoparticles: a novel graded SERS substrate, *J. Phys. Chem. C* 111 (2007) 16167–16173, <https://doi.org/10.1021/jp073771z>.
- [39] Q. Zhou, J. Zheng, Z. Qing, M. Zheng, J. Yang, S. Yang, et al., Detection of circulating tumor DNA in human blood via DNA-mediated surface-enhanced Raman spectroscopy of single-walled carbon nanotubes, *Anal. Chem.* 88 (2016) 4759–4765, <https://doi.org/10.1021/acs.analchem.6b00108>.
- [40] A. Kinkhabwala, Z. Yu, S. Fan, Y. Avlasevich, K. Müllen, W.E. Moerner, Large single-molecule fluorescence enhancements produced by a bowtie nanoantenna, *Nat. Photonics* 3 (2009) 654–657, <https://doi.org/10.1038/nphoton.2009.187>.
- [41] Y. Luo, X. He, Y. Kim, J.L. Blackburn, S.K. Doorn, H. Htoon, et al., Carbon nanotube color centers in plasmonic nanocavities: a path to photon indistinguishability at telecom bands, *Nano Lett* (2019), <https://doi.org/10.1021/acs.nanolett.9b04069>.
- [42] M. Glaeske, A. Setaro, Nanoplasmonic colloidal suspensions for the enhancement of the luminescence emission from single-walled carbon nanotubes, *Nano Res* 6 (2013) 593–601, <https://doi.org/10.1007/s12274-013-0335-5>.
- [43] J. Yang, Q. Zhao, M. Lyu, Z. Zhang, X. Wang, M. Wang, et al., Chirality-selective photoluminescence enhancement of ssDNA-wrapped single-walled carbon nanotubes modified with gold nanoparticles, *Small* 12 (2016) 3164–3171, <https://doi.org/10.1002/sml.201503883>.
- [44] S.J. Kim, J. Park, Y. Jeong, H. Go, K. Lee, S. Hong, et al., Metal-particle-induced enhancement of the photoluminescence from biomolecule-functionalized carbon nanotubes, *Nanoscale Res. Lett.* 9 (2014) 1–7, <https://doi.org/10.1186/1556-276X-9-85>.
- [45] M. Glaeske, A. Setaro, Effect of hybrid isolation on the luminescence enhancement of carbon nanotube-gold nanorod composites, *Phys. Status Solidi* 251 (2014) 2480–2484, <https://doi.org/10.1002/pssb.201451288>.
- [46] A. Amirjani, N.N. Koochak, D.F. Haghshenas, Synthesis of silver nanotriangles with tunable edge length: a promising candidate for light harvesting purposes within visible and near-infrared ranges, *Mater. Res. Express* 6 (2019), 036204, <https://doi.org/10.1088/2053-1591/aaf624>.
- [47] A. Amirjani, D.F. Haghshenas, Ag nanostructures as the surface plasmon resonance (SPR)-based sensors: a mechanistic study with an emphasis on heavy metallic ions detection, *Sensor. Actuator. B Chem.* 273 (2018) 1768–1779, <https://doi.org/10.1016/j.snb.2018.07.089>.
- [48] S. Kruss, D.P. Salem, L. Vuković, B. Lima, E. Vander Ende, E.S. Boyden, et al., High-resolution imaging of cellular dopamine efflux using a fluorescent nanosensor array, *Proc. Natl. Acad. Sci. U.S.A.* 114 (2017) 1789–1794, <https://doi.org/10.1073/pnas.1613541114>.
- [49] R.M. Williams, C. Lee, D.A. Heller, A fluorescent carbon nanotube sensor detects the metastatic prostate cancer biomarker uPA, *ACS Sens.* 3 (2018) 1838–1845, <https://doi.org/10.1021/acssensors.8b00631>.
- [50] B. Liu, F. Wu, H. Gui, M. Zheng, C. Zhou, Chirality-Controlled synthesis and applications of single-walled carbon nanotubes, *ACS Nano* 11 (2017) 31–53, <https://doi.org/10.1021/acsnano.6b06900>.
- [51] V. Zubkovs, A. Antonucci, N. Schuergers, B. Lambert, A. Latini, R. Ceccarelli, et al., Spinning-disc confocal microscopy in the second near-infrared window (NIR-II), *Sci. Rep.* 8 (2018) 13770, <https://doi.org/10.1038/s41598-018-31928-y>.
- [52] T.V. Tsoulos, L. Fabris, Interface and bulk standing waves drive the coupling of plasmonic nanostar antennas, *J. Phys. Chem. C* 122 (2018) 28949–28957, <https://doi.org/10.1021/acs.jpcc.8b09263>.
- [53] T.V. Tsoulos, L. Han, J. Weir, H.L. Xin, L. Fabris, A closer look at the physical and optical properties of gold nanostars: an experimental and computational study, *Nanoscale* 9 (2017) 3766–3773, <https://doi.org/10.1039/c6nr09091e>.
- [54] P.B. Johnson, R.W. Christy, Optical constants of the noble metals, *Phys. Rev. B* 6 (1972) 4370–4379, <https://doi.org/10.1103/PhysRevB.6.4370>.
- [55] G.M. Hale, M.R. Querry, Optical constants of water in the 200-nm to 200- μ m wavelength region, *Appl. Opt.* 12 (1973) 555–563, <https://doi.org/10.1364/ao.12.000555>.
- [56] N.K. Emani, T.F. Chung, A.V. Kildishev, V.M. Shalae, Y.P. Chen, A. Boltasseva, Electrical modulation of fano resonance in plasmonic nanostructures using graphene, *Nano Lett* 14 (2014) 78–82, <https://doi.org/10.1021/nl403253c>.
- [57] N.K. Emani, T.F. Chung, X. Ni, A.V. Kildishev, Y.P. Chen, A. Boltasseva, Electrically tunable damping of plasmonic resonances with graphene, *Nano Lett* 12 (2012) 5202–5206, <https://doi.org/10.1021/nl302322t>.
- [58] D. Rioux, S. Vallières, S. Besner, P. Muñoz, E. Mazur, M. Meunier, An analytic model for the dielectric function of Au, Ag, and their alloys, *Adv. Opt. Mater.* 2 (2014) 176–182, <https://doi.org/10.1002/adom.201300457>.
- [59] C.M. Cobley, S.E. Skrabalak, D.J. Campbell, Y. Xia, Shape-controlled synthesis of silver nanoparticles for plasmonic and sensing applications, *Plasmonics* 4 (2009) 171–179, <https://doi.org/10.1007/s11468-009-9088-0>.
- [60] H. Huang, R. Maruyama, K. Noda, H. Kajiuira, K. Kadono, Preferential destruction of metallic single-walled carbon nanotubes by laser irradiation, *J. Phys. Chem. B* 110 (2006) 7316–7320, <https://doi.org/10.1021/jp056684k>.
- [61] A.V. Naumov, S. Ghosh, D.A. Tsybouski, S.M. Bachilo, R.B. Weisman, Analyzing absorption backgrounds in single-walled carbon nanotube spectra, *ACS Nano* 5 (2011) 1639–1648, <https://doi.org/10.1021/nn103592z>.
- [62] M.J. O'Connell, S.H. Bachilo, C.B. Huffman, V.C. Moore, M.S. Strano, E.H. Haroz, et al., Band gap fluorescence from individual single-walled carbon nanotubes, *Science* 297 (2002) 593–596, <https://doi.org/10.1126/science.1072631>, 80–.
- [63] P. Anger, P. Bharadwaj, L. Novotny, Enhancement and quenching of single-molecule fluorescence, *Phys. Rev. Lett.* 96 (2006) 113002, <https://doi.org/10.1103/PhysRevLett.96.113002>.
- [64] M. Glaeske, M. Kumar, T. Bisswanger, S. Vaitiekėnas, C. Soci, R. Narula, et al., Relaxation lifetimes of plasmonically enhanced hybrid gold-carbon nanotubes systems, *Nanotechnology* 28 (2017) 255202, <https://doi.org/10.1088/1361-6528/aa7409>.
- [65] K. Matsuda, Y. Ito, Y. Kanemitsu, Photoluminescence enhancement and quenching of single CdSeZnS nanocrystals on metal surfaces dominated by plasmon resonant energy transfer, *Appl. Phys. Lett.* 92 (2008) 211911, <https://doi.org/10.1063/1.2937142>.
- [66] H. Ashiba, Y. Iizumi, T. Okazaki, X. Wang, M. Fujimaki, Carbon nanotubes as fluorescent labels for surface plasmon resonance-assisted flowimmunoassay, *Sensors* 17 (2017) 2569, <https://doi.org/10.3390/s17112569>.
- [67] Z. Shi, X. Hong, H.A. Bechtel, B. Zeng, M.C. Martin, K. Watanabe, et al., Observation of a Luttinger-liquid plasmon in metallic single-walled carbon nanotubes, *Nat. Photonics* 9 (2015) 515–519, <https://doi.org/10.1038/nphoton.2015.123>.
- [68] L.D. Filip, V. Filip, Influence of electron quantum confinement on the strength of carbon nanotube bundles, *Solid State Electron. Lett.* 1 (2019) 1–9, <https://doi.org/10.1016/j.ssel.2018.09.001>.
- [69] M.A. Huergo, C.M. Maier, M.F. Castez, C. Vericat, S. Nede, R.C. Salvarezza, et al., Optical nanoparticle sorting elucidates synthesis of plasmonic nanotriangles, *ACS Nano* 10 (2016) 3614–3621, <https://doi.org/10.1021/acsnano.5b08095>.
- [70] Y. Ren, H. Qi, Q. Chen, S. Wang, L. Ruan, Localized surface plasmon resonance of nanotriangle dimers at different relative positions, *J. Quant. Spectrosc. Radiat. Transf.* 199 (2017) 45–51, <https://doi.org/10.1016/j.jqsrt.2017.05.003>.
- [71] S. Fayyaz, M. Tabatabaei, R. Hou, F. Lagugné-Labarthe, Surface-enhanced fluorescence: mapping individual hot spots in silica-protected 2D gold nanotriangle arrays, *J. Phys. Chem. C* 116 (2012) 11665–11670, <https://doi.org/10.1021/jp302191z>.
- [72] C. Hrelescu, T.K. Sau, A.L. Rogach, F. Jäckel, G. Laurent, L. Douillard, et al., Selective excitation of individual plasmonic hotspots at the tips of single gold nanostars, *Nano Lett* 11 (2011) 402–407, <https://doi.org/10.1021/nl103007m>.
- [73] B.C. Galarreta, I. Rugar, A. Young, F. Lagugné-Labarthe, Mapping hot-spots in hexagonal arrays of metallic nanotriangles with azobenzene polymer thin films, *J. Phys. Chem. C* 115 (2011) 15318–15323, <https://doi.org/10.1021/jp204402f>.
- [74] B. Kozinsky, N. Marzari, Static dielectric properties of carbon nanotubes from first principles, *Phys. Rev. Lett.* 96 (2006) 166801, <https://doi.org/10.1103/PhysRevLett.96.166801>.
- [75] E.N. Brothers, G.E. Scuseria, K.N. Kudin, Longitudinal polarizability of carbon nanotubes, *J. Phys. Chem. B* 110 (2006) 12860–12864, <https://doi.org/10.1021/jp0603839>.
- [76] E.N. Brothers, A.F. Izmaylov, G.E. Scuseria, K.N. Kudin, Analytically calculated polarizability of carbon nanotubes: single wall, coaxial, and bundled systems, *J. Phys. Chem. C* 112 (2008) 1396–1400, <https://doi.org/10.1021/jp709931r>.
- [77] M. Takase, H. Ajiki, Y. Mizumoto, K. Komeda, M. Nara, H. Nabika, et al., Selection-rule breakdown in plasmon-induced electronic excitation of an isolated single-walled carbon nanotube, *Nat. Photonics* 7 (2013) 550–554, <https://doi.org/10.1038/nphoton.2013.129>.
- [78] A.R. Amori, J.E. Rossi, B.J. Landi, T.D. Krauss, Defects enable dark exciton photoluminescence in single-walled carbon nanotubes, *J. Phys. Chem. C* 122 (2018) 3599–3607, <https://doi.org/10.1021/acs.jpcc.7b10565>.
- [79] L. Huang, H.N. Pedrosa, T.D. Krauss, Ultrafast ground-state recovery of single-walled carbon nanotubes, *Phys. Rev. Lett.* 93 (2004), 017403, <https://doi.org/10.1103/PhysRevLett.93.017403>.
- [80] Y.Z. Ma, J. Stenger, J. Zimmermann, S.M. Bachilo, R.E. Smalley, R.B. Weisman, et al., Ultrafast carrier dynamics in single-walled carbon nanotubes probed by femtosecond spectroscopy, *J. Chem. Phys.* 120 (2004) 3368–3373, <https://doi.org/10.1063/1.1640339>.
- [81] S. Lebedkin, F. Hennrich, O. Kiowski, M.M. Kappes, Photophysics of carbon nanotubes in organic polymer-toluene dispersions: emission and excitation satellites and relaxation pathways, *Phys. Rev. B Condens. Matter* 77 (2008) 165429, <https://doi.org/10.1103/PhysRevB.77.165429>.
- [82] K.E. Fong, L.Y.L. Yung, Localized surface plasmon resonance: a unique property of plasmonic nanoparticles for nucleic acid detection, *Nanoscale* 5 (2013) 12043–12071, <https://doi.org/10.1039/c3nr02257a>.
- [83] A.L. Feng, M.L. You, L. Tian, S. Singamaneni, M. Liu, Z. Duan, et al., Distance-dependent plasmon-enhanced fluorescence of upconversion nanoparticles using polyelectrolyte multilayers as tunable spacers, *Sci. Rep.* 5 (2015) 1–10, <https://doi.org/10.1038/srep07779>.

- [84] J.J. Mock, R.T. Hill, A. Degiron, S. Zauscher, A. Chilkoti, D.R. Smith, Distance-dependent plasmon resonant coupling between a gold nanoparticle and gold film, *Nano Lett* 8 (2008) 2245–2252, <https://doi.org/10.1021/nl080872f>.
- [85] D. Alba-Molina, M. Martín-Romero, L. Camacho, J. Giner-Casares, Ion-mediated aggregation of gold nanoparticles for light-induced heating, *Appl. Sci.* 7 (2017) 916, <https://doi.org/10.3390/app7090916>.
- [86] Q. Xiliang, C. Yang, L. Tiesong, H. Peng, W. Jun, L. Ping, et al., Large-scale synthesis of silver nanoparticles by aqueous reduction for low-temperature sintering bonding, *J. Nanomater.* 2014 (2014), <https://doi.org/10.1155/2014/594873>.
- [87] H. Hirai, N. Yakura, Protecting polymers in suspension of metal nanoparticles, *Polym. Adv. Technol.* 12 (2001) 724–733, <https://doi.org/10.1002/pat.95>.
- [88] Y.T. Cheng, R.H. Uang, K.C. Chiou, Effect of PVP-coated silver nanoparticles using laser direct patterning process by photothermal effect, *Microelectron. Eng.* 88 (2011) 929–934, <https://doi.org/10.1016/j.mee.2010.12.020>.
- [89] X. Wang, W. Fan, Z. Dong, D. Liang, T. Zhou, Interactions of natural organic matter on the surface of PVP-capped silver nanoparticle under different aqueous environment, *Water Res* 138 (2018) 224–233, <https://doi.org/10.1016/j.watres.2018.03.048>.
- [90] N.S. Abadeer, M.R. Brennan, W.L. Wilson, C.J. Murphy, Distance and plasmon wavelength dependent fluorescence of molecules bound to silica-coated gold nanorods, *ACS Nano* 8 (2014) 8392–8406, <https://doi.org/10.1021/nl502887j>.
- [91] D.P. Salem, X. Gong, A.T. Liu, V.B. Koman, J. Dong, M.S. Strano, Ionic strength-mediated phase transitions of surface-adsorbed DNA on single-walled carbon nanotubes, *J. Am. Chem. Soc.* 139 (2017) 16791–16802, <https://doi.org/10.1021/jacs.7b09258>.
- [92] A.J. Gillen, J. Kupis-Rozmysl Owicz, C. Gigli, N. Schuergers, A.A. Boghossian, Xeno nucleic acid nanosensors for enhanced stability against ion-induced perturbations, *J. Phys. Chem. Lett.* 9 (2018) 4336–4343, <https://doi.org/10.1021/acs.jpcclett.8b01879>.
- [93] X. Tu, M. Zheng, A DNA-based approach to the carbon nanotube sorting problem, *Nano Res* 1 (2008) 185–194, <https://doi.org/10.1007/s12274-008-8022-7>.
- [94] J. McMorro, M. Freeley, M. Palma, DNA-wrapped single-walled carbon nanotube Assemblies, *Ind. Eng. Chem. Res.* 56 (2017) 5302–5308, <https://doi.org/10.1021/acs.iecr.7b00429>.
- [95] Y. Yang, A. Sharma, G. Noetinger, M. Zheng, A. Jagota, Pathway-dependent structures of DNA-wrapped carbon nanotubes: direct sonication vs surfactant/DNA exchange, *J. Phys. Chem. C* 124 (2020) 9045–9055, <https://doi.org/10.1021/acs.jpcc.0c00679>.
- [96] Y. Yang, A. Shankar, T. Aryaksama, M. Zheng, A. Jagota, Quantification of DNA/SWCNT solvation differences by aqueous two-phase separation, *Langmuir* 34 (2018) 1834–1843, <https://doi.org/10.1021/acs.langmuir.7b03186>.
- [97] B. Lambert, A.J. Gillen, N. Schuergers, S.J. Wu, A.A. Boghossian, Directed evolution of the optoelectronic properties of synthetic nanomaterials, *Chem. Commun.* 55 (2019) 3239–3242, <https://doi.org/10.1039/c8cc08670b>.
- [98] M.P. Landry, L. Vuković, S. Kruss, G. Bisker, A.M. Landry, S. Islam, et al., Comparative dynamics and sequence dependence of DNA and RNA binding to single walled carbon nanotubes, *J. Phys. Chem. C* 119 (2015) 10048–10058, <https://doi.org/10.1021/jp511448e>.
- [99] J.H. Kim, C.R. Patra, J.R. Arkalgud, A.A. Boghossian, J. Zhang, J.H. Han, et al., Single-molecule detection of H₂O₂ mediating angiogenic redox signaling on fluorescent single-walled carbon nanotube array, *ACS Nano* 5 (2011) 7848–7857, <https://doi.org/10.1021/nn201904t>.
- [100] J.D. Harvey, P.V. Jena, H.A. Baker, G.H. Zerze, R.M. Williams, T.V. Galassi, et al., A carbon nanotube reporter of microRNA hybridization events in vivo, *Nat. Biomed. Eng.* 1 (2017) 41, <https://doi.org/10.1038/s41551-017-0041>.
- [101] S. Sen, F. Sen, A.A. Boghossian, J. Zhang, M.S. Strano, Effect of reductive dithiothreitol and trolox on nitric oxide quenching of single-walled carbon nanotubes, *J. Phys. Chem. C* 117 (2013) 593–602, <https://doi.org/10.1021/jp307175f>.
- [102] P.W. Barone, S. Baik, D.A. Heller, M.S. Strano, Near-infrared optical sensors based on single-walled carbon nanotubes, *Nat. Mater.* 4 (2005) 86–92, <https://doi.org/10.1038/nmat1276>.
- [103] A. Amirjani, N.N. Koochak, D.F. Haghshenas, Investigating the shape and size-dependent optical properties of silver nanostructures using UV-vis spectroscopy, *J. Chem. Educ.* 96 (2019) 2584–2589, <https://doi.org/10.1021/acs.jchemed.9b00559>.
- [104] A. Amirjani, F. Firouzi, D.F. Haghshenas, Predicting the size of silver nanoparticles from their optical properties, *Plasmonics* 15 (2020) 1077–1082, <https://doi.org/10.1007/s11468-020-01121-x>.
- [105] B.P. Lambert, A.J. Gillen, A.A. Boghossian, Synthetic biology: a solution for tackling nanomaterial challenges, *J. Phys. Chem. Lett.* 11 (2020) 4791–4802, <https://doi.org/10.1021/acs.jpcclett.0c00929>.
- [106] M. Lyu, B. Meany, J. Yang, Y. Li, M. Zheng, Toward complete resolution of DNA/carbon nanotube hybrids by aqueous two-phase systems, *J. Am. Chem. Soc.* 141 (2019) 20177–20186, <https://doi.org/10.1021/jacs.9b09953>.
- [107] J.T. Glückert, L. Adamska, W. Schinner, M.S. Hofmann, S.K. Doorn, S. Tretiak, et al., Dipolar and charged localized excitons in carbon nanotubes, *Phys. Rev. B* 98 (2018), 195413, <https://doi.org/10.1103/PhysRevB.98.195413>.
- [108] V.A. Shahnazaryan, V.A. Saroka, I.A. Shelykh, W.L. Barnes, M.E. Portnoi, Strong light-matter coupling in carbon nanotubes as a route to exciton brightening, *ACS Photonics* 6 (2019) 904–914, <https://doi.org/10.1021/acsphotonics.8b01543>.
- [109] A. Ishii, H. Machiya, Y.K. Kato, High efficiency dark-to-bright exciton conversion in carbon nanotubes, *Phys. Rev. X* 9 (2019), 041048, <https://doi.org/10.1103/PhysRevX.9.041048>.